Multifunctional Bi$_2$S$_3$-Au nanoclusters for fluorescence/infrared thermal imaging guided photothermal therapy

Hongmei Sun [a], Yuyu Cao [a], Beibei Zhai [a], Xiaoshuang Zhao [a], Xuejun Zhang [a,b,c], Jiangtao Su [a,*]

[a] National '111' Center for Cellular Regulation and Molecular Pharmaceutics, Key Laboratory of Fermentation Engineering (Ministry of Education), Key Laboratory of Industrial Microbiology in Hubei, Cooperative Innovation Center of Industrial Fermentation (Ministry of Education & Hubei Province), School of Life Science and Health, Hubei University of Technology, Wuhan 430068, China
[b] Hubei Bio-Pharmaceutical Industrial-Technological Institute Inc., Wuhan, Hubei 430075, China
[c] Humanwell Healthcare (Group) Co., Ltd., Wuhan, Hubei 430075, China

ARTICLE INFO

ABSTRACT

Nanotechnology has attracted extensive attention in the diagnosis and treatment of cancer. Therefore, the research aimed at developing new nanomaterials and exploring their applications in biomedicine has attracted more attention. In this study, Bi$_2$S$_3$-Au nanoclusters (Bi$_2$S$_3$-AuNCs) as fluorescence/infrared thermal imaging-guided photothermal therapy (PTT) was prepared for the first time. It was achieved in a facile and mild way by optimizing the amount of Bi^{3+} and Au^{3+} using bovine serum albumin (BSA) as reducer and stabilizer. The as-prepared Bi$_2$S$_3$-AuNCs with special morphology showed high stability, excellent biocompatibility and good photostability. Apart from these, it also can accumulate at tumor sites and exhibit considerable fluorescence/infrared thermal imaging-guided PTT. Bi$_2$S$_3$-AuNCs nanoparticles integrate imaging and therapeutic functions into an advanced application platform, which provides the possibility to build a novel nano-cancer diagnosis and treatment platform.

1. Introduction

Cancer is the leading cause of human death (Siegel et al., 2022; Todd, 2023), and traditional cancer treatments (such as surgery, radiotherapy and chemotherapy) still fail to meet the expectations of patients and the medical community (Nguyen et al., 2023; Roncevic et al., 2023). Developing new diagnosis and treatment of cancer is beneficial to improve the treatment effect and prolong the survival time of patients (Dong et al., 2023; Guhaniyogi, 2023). Photothermal therapy as a new cancer treatment can convert light energy into heat under the irradiation of a near-infrared light source (Sheng et al., 2023), thereby raising the temperature of the surrounding environment to kill cancer cells (Chansaenpak et al., 2023; Chen et al., 2023a). It can precisely target to the tumor site, thus minimizing the extent of damage to surrounding healthy tissue (Chai et al., 2023). Particularly, photothermal therapy can repress tumor cell migration and metastasis by weakening adhesion force and biomechanical property of tumor cells (Baranwal et al., 2023; Freitas et al., 2023). There are many nanomaterials with photothermal functions, including precious metals, semiconductors (Wen et al., 2022; Wang et al., 2023), organic materials and so on(Bobo et al., 2016; Deng

et al., 2023). Among these nanomaterials, bismuth sulfide, as a common semiconductor nanomaterial with low price (Shahbazi et al), simple synthesis method and high X-ray attenuation coefficient, has been reported as an efficient photothermal agent (Ai et al., 2011; Yang et al., 2023; Zheng et al., 2015). As two is better than one, combine different nanomaterials together to develop the efficient photothermal therapy platform has attracted great interest of scientists (Liu et al., 2019; Wang et al., 2020). In previous work, our group also prepared Au/Bi$_2$S$_3$ nanoflowers for efficient photothermal therapy. With the coordination of Au and Bi$_2$S$_3$, the photothermal performance of this nanoflowers is higer than single Au and Bi$_2$S$_3$ nanoparticles (Zhao et al., 2020). Although great progress have been made in the development of new therapy of cancer, it still lack of efficient diagnostic and tracking methods for precise treatment and real-time monitoring of tumors (Alibakhshi et al., 2017; Katifelis and Gazouli, 2021).

Recently, imaging guide-photothermal therapy has received increasing attention as it can not only enhance the accuracy of diagnosis, but also visualize the situation of the tumor during treatment (Chen et al., 2016; Zhang et al., 2019). Many imaging modalities such as photoacoustic (PA) imaging (Christie et al., 2023), magnetic resonance
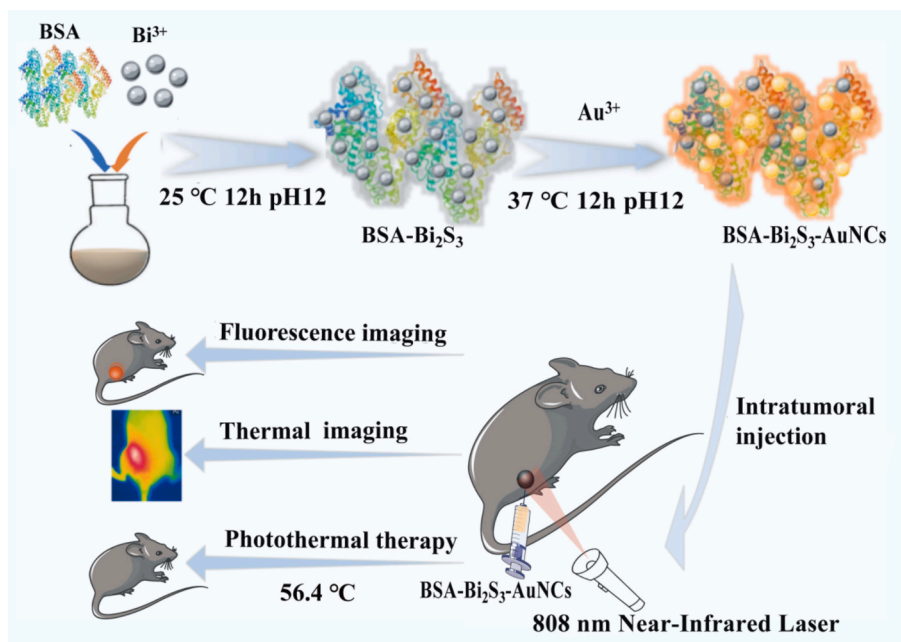
---

* Corresponding author.
  E-mail address: jiangtsu@hbut.edu.cn (J. Su).

Scheme 1. Schematic illustration of the design process of Bi$_2$S$_3$-AuNCs.

imaging (MRI), CT imaging and infrared thermal (IRT) imaging, enabling diagnosis guidance and therapeutic monitoring (Djajakusumah et al., 2023; Du et al., 2023). Among various imaging modalities, fluorescence imaging is considered as a powerful way to distinguish the tumor site from normal tissues (Hu et al., 2023; (Thapa et al., 2023). Many NIR probes have been developed as it could offer a desirable signal-to-background ratio and tissue-penetration depth (Wu et al., 2023). However, the special camera and systematic training required for NIR probes usage further limit the use of these probes in clinical (de la Fleche et al., 2023). Therefore, visual fluorescence imaging-guide photothermal therapy are highly demanded.

Bovine serum albumin (BSA)-stabilized gold nanoclusters (AuNCs) with a bright red fluorescence under 365 nm UV light has attracted great attention due to their fascinating properties, such as highly luminescence, low photo-bleaching, non-toxicity as well as good biocompatibility (Chen et al., 2023b; Nosrati et al., 2022; Zhao et al., 2020; Jiang et al., 2024). With these in mind, we report herein the first example of the preparation of Bi$_2$S$_3$-AuNCs nanocomposites with red fluorescence (Scheme 1). Several advantages of these nanocomposites make them especially attractive. First, the as-prepared nanomaterials are fabricated using a low-cost, non-toxic and facile synthetic route. Second, the composition of Bi$_2$S$_3$-AuNCs provides the nanocomposites with the capability of dual-modal visible fluorescence and NIR thermal imaging at low concentration. Third, the as-prepared nanocomposites with good biocompatibility and stability exhibited high photothermal conversion efficiency. Finally, the combination of visible fluorescence and NIR thermal dual-modal imaging with photothermal therapy provides a new versatile platform for the exploration of theranostic agents for early diagnosis and treatment of cancer.

2. Experimental part

2.1. Materials

Bovine serum albumin (BSA) and dimethyl sulfoxide (DMSO, for molecular biology) was obtained from Biofroxx. Nitric acid (HNO$_3$, 65–68 %). Bismuth nitrate pentahydrate (Bi(NO$_3$)$_3$·5H$_2$O), sodium hydroxide (NaOH), chloroauric acid (HAuCl$_4$•4H$_2$O), paraformaldehyde was purchased from Sinopharm Chemial Reagent Co., Ltd. DMEM/High glucose, Penicillin-Streptomycin solution, phosphote buffered saline

(PBS) and thiazolyl blue (MTT) were purchased from HyCloneTM. 0.25 % trypsin-EDTA was purchased from Gibco. Fetal Bovine Serum (FBS) was obtained from Every Green. DAPI Staining Solution was obtained from Beyotime. The mouse melanoma cell (B16F10) were purchased from Beijing Beina Chuanglian Biotechnology Research Institute (BNCC). Female C57BL/6 mice (8 weeks old) were purchased from the Laboratory Animal Center of Huazhong Agricultural Univer-sity.

2.2. Nanomaterials preparation

2.2.1. Preparation of Bi$_2$S$_3$ nanoparticles

BSA-mediated Bi$_2$S$_3$ nanoparticles were prepared using the biomineralization approach described by Yong Wang and his coworkers. Briefly, 250 mg of BSA and 0.5 mg of Bi(NO$_3$)$_3$·5H$_2$O was dissolved in 8.0 mL of Milli-Q water and 1.0 mL of HNO$_3$ (2 M), respectively. Then Bi (NO$_3$)$_3$ solution was added into BSA solution and stirred at 25 °C for 30 min. Next, the pH of the solution was adjusted to 12 using NaOH (2 M), and the mixture was stirred for 12 h. The obtained Bi$_2$S$_3$ nanoparticles were dialyzed (molecular weight cut off = 14,000) against Milli-Q water for 12 h to remove the excess ions.

2.2.2. Preparation of Bi$_2$S$_3$-AuNCs nanoparticles

1 mL of HAuCl$_4$ (50 mM) was added to the Bi$_2$S$_3$ solution prepared above and stirred vigorously for about 2 min at 37 °C. The solution was adjusted to pH = 12 using NaOH (2 M). Then the mixture was stirred for 12 h followed by dialysis for 12 h. Bi$_2$S$_3$-AuNCs was collected by centrifugation.

2.3. Characterization

The morphology of as-prepared Bi$_2$S$_3$-AuNCs was detected by Transmission electron microscopy (TEM, JEOL 2000-FX). The element mapping was carried out by Energy-dispersive spectroscopy (EDS, FEI TALOS F200). Particularly, the Bright-Field (BF) image was recorded using a phase contrast detector. And the Dark-Field image was taken with a High-Angle Annular Dark-Field (HAADF) detector at an electron acceleration voltage of 200 kV. The size and zeta potential were measured by a Zetasizer Nano ZS apparatus (Malvern Instruments, United Kingdom). The optical properties were analyzed by UV–vis-NIR absorption spectra (UV, SHIMADZU UV1800). X-ray diffraction (XRD,
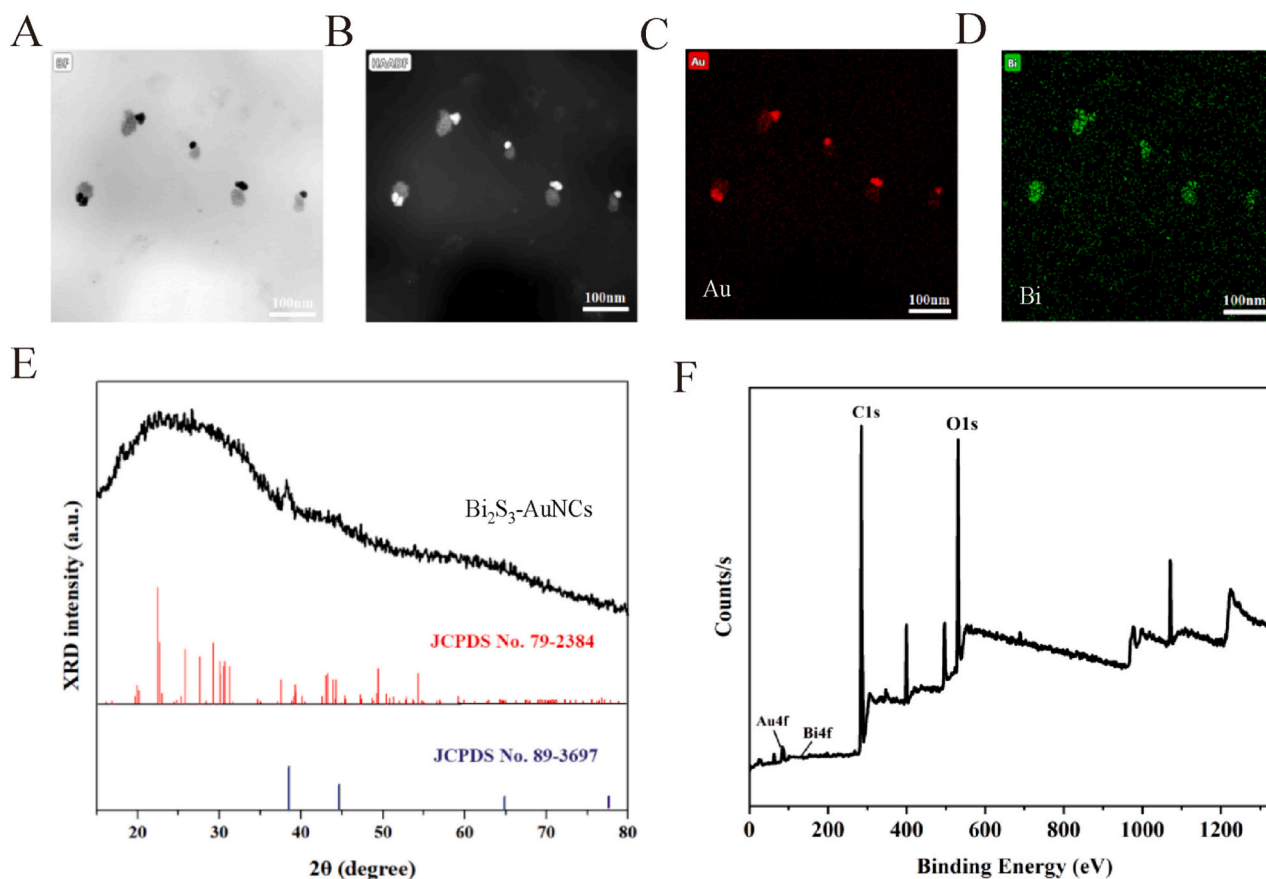
Fig. 1. STEM-EDS element mapping (A) Bright Filed; (B) High-Angle Annular Dark Field; (C) Au element; (D) Bi element) of Bi_2S_3-AuNCs. (E) XRD image of Bi_2S_3-AuNCs (JCPDS No.79–2384 is the standard card of Bi_2S_3, JCPDS No.89–3697 is the standard card of Au). (F) full scan XPS survey spectrum of Bi_2S_3-AuNCs.

Rigaku Corporation Ultima IV) characterization was performed to analysis the crystal structure. The atomic ration of Bi and Au was investigated by Inductively Coupled Plasma Optical Emission Spectrometer (ICP-OES, Agilent ICPOES730). The chemical compositions of Bi_2S_3-AuNCs were determined by X-ray Photoelectron Spectroscopy (XPS, Thermo ESCALAB 250xi). ThermoGravimetric Analysis (TGA, TA_60WS) was conducted with thermo-analyzer instrument from room temperature to 800 °C at a heating rate of 10 °C/min. The infrared spectroscopy and fluorescence intensity were measured by the Fourier Transform Infrared Spectrometer (FTIR, Bruker Optics VERTEX70) and Fluorospectrophotometer (SHIMADZU RF-6000) respectively. Fluorescence images were obtained from Fluorescent Inverted Microscope (Olympus Corporation, IX73) and In Vivo Imaging Systems (IVIS Lumina XRMS Series III). MTT absorbance was measured by Enzyme-Labeled Instrument (Bio Tech).

2.3.1. Photothermal experiment

Bi_2S_3-AuNCs with different concentrations were irradiated under 808 nm laser for 10 min. The temperature was recorded every 30 s.

To calculate the photothermal conversion efficiency of the Bi_2S_3-AuNCs composite, heating up and cooling curve were measured.

2.3.2. Fluorescence intensity of Bi_2S_3-AuNCs

To examine the fluorescence intensity of Bi_2S_3-AuNCs, different concentrations of Bi_2S_3-AuNCs were prepared. The emission and the excitation spectrum were plotted respectively.

2.3.3. Cytotoxicity and photothermal performance in vitro

B16F10 cell was cultured at 37 °C in dulbecco's modified eagle medium (DMEM) containing 10 % fetal bovine serum. The

biocompatibility and photothermal property of Bi_2S_3-AuNCs in vitro were performed by MTT experiment. The cells were incubated with different concentrations of Bi_2S_3 NPs (0–4.0 μg/mL for Bi), AuNCs (0–47 μg/mL for Au), Bi_2S_3 + AuNCs (0–4.0 μg/mL for Bi, 0–47 μg/mL for Au) and Bi_2S_3-AuNCs (0–4.0 μg/mL for Bi) for 24 h. The absorbance was measured using an Enzyme-Labeled Instrument. For photothermal assessment, B16F10 cells were incubated with Bi_2S_3 NPs, AuNCs, Bi_2S_3 + AuNCs and Bi_2S_3-AuNCs solution for 4 h, and then the solutions were irradiated for 2 min (2.0 W/cm^2). Followed by 20 h incubation, the cell viability was calculated according to MTT results.

2.3.4. Intracellular uptake of Bi_2S_3-AuNCs with B16F10 cells

B16F10 cells were seeded in a 6-well plate with 2×10^5 cells per well, The medium was 2 mL/well. After incubation for 24 h, PBS solution was used to clean for 2 times and 2 mL of Bi_2S_3-AuNCs with different concentrations (C_{Bi} = 1.0, 2.0 and 4.0 μg/mL) was added to each well. The medium in the wells was aspirated out and washed once using PBS; 1 mL of paraformaldehyde was added to each well for fixation for 15 min. The paraformaldehyde solution was aspirated and washed once using PBS, and 400 μL DAPI dye solution was added to each well, stained for 5 min, and the DAPI dye solution was aspirated and washed 1–2 times using PBS. Blue and red fluorescence were observed under an inverted fluorescence microscope. Similarly, Bi_2S_3-AuNCs at a certain concentration (C_{Bi} = 4.0 μg/mL) was incubated with B16F10 cells for 1, 4, 8 h, and the fluorescence was observed under an inverted fluorescence microscope as described above.

2.3.5. Animal tumor model

All animal experiments were conducted in accordance with the regulations and guidelines of Hubei University of Technology (Ethics
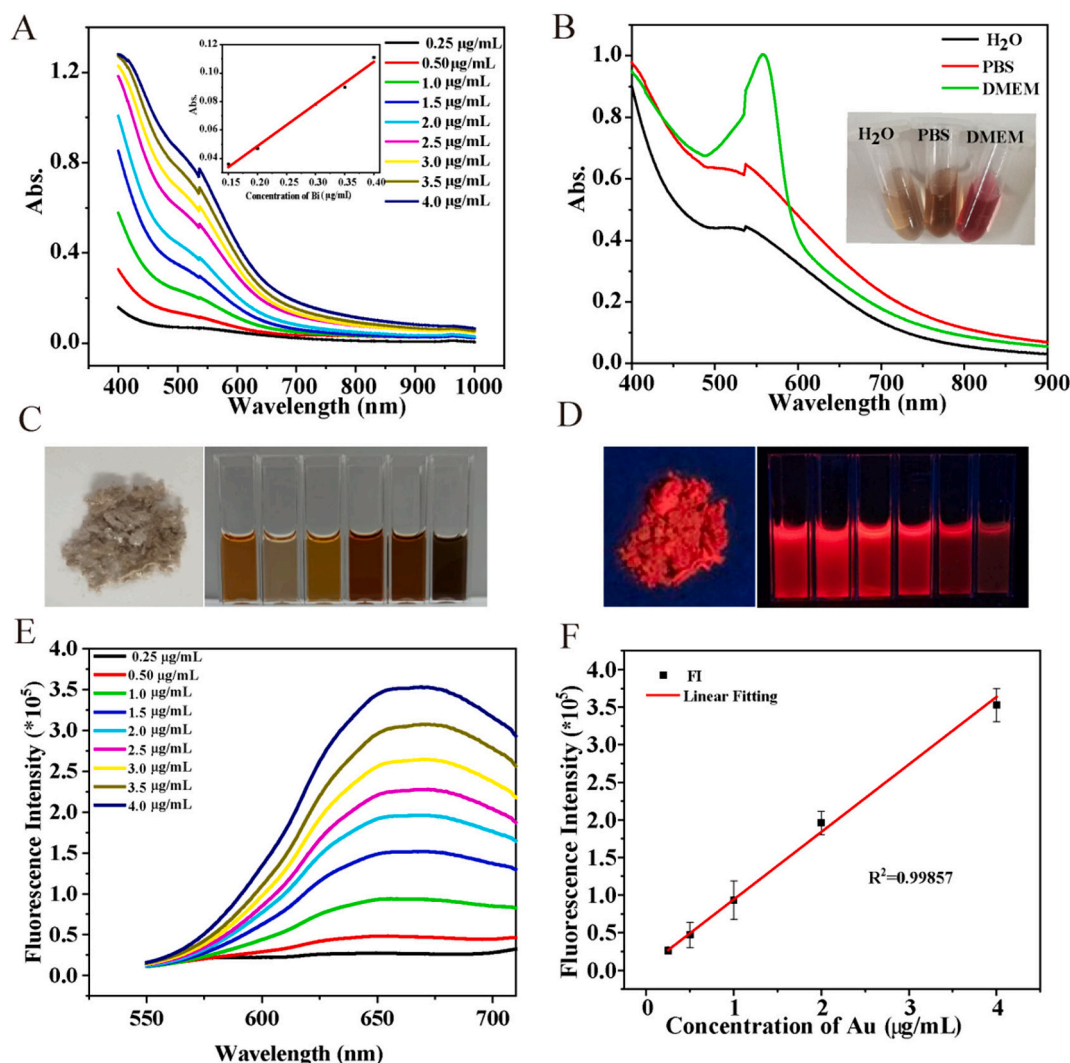
Fig. 2. (A) UV–vis spectrua of different concentrations of Bi$_2$S$_3$-AuNCs (Insert is the linear fitting curve of concentrations-808 nm absorption values of Bi$_2$S$_3$-AuNCs). - (B) UV–vis spectra of Bi$_2$S$_3$-AuNCs dissolved in different solvents (H$_2$O , PBS, DMEM) (Insert is the electronic pictures of Bi$_2$S$_3$-AuNCs dissolved in different solvents). Photos of lyophilized solid and solution of Bi$_2$S$_3$-AuNCs in day light (C) and and under 365 nm light (D) (The solutions from left to right are Bi$_2$S$_3$-AuNCs prepared with 0, 0.25 mg, 0.5 mg, 1.0 mg, 1.25 mg and 1.5 mg of Bi(NO$_3$)$_3$·5H$_2$O, respectively). (E) Emission spectra (λ_{em} = 670 nm) of different concenetrations of Bi$_2$S$_3$-AuNCs. (F) Linear fitting curve of concentrations-fluorescence intensities of Bi$_2$S$_3$-AuNCs.

approval No. HBUT20230085), and adheres to ARRIVE (Animal Research: Reporting of In Vivo Experiments) guidelines. B16F10 cells in PBS were injected into the right side of the inner thigh of female C57BL/6 mice (weight: 25–30 g) aged 4–5 weeks. When tumors grew to 100 mm^3, tumor-bearing mice were used for subsequent experiments.

Tumor volume = (tumor length) × (tumor width) ^{2}/2.

2.3.6. Evaluation of the photothermal therapy in vivo

Tumor bearing mice were divided into six groups. Group 1: Intra-tumoral injection 100 μl of PBS. Group 2: Intratumoral injection 100 μl of PBS under 808 nm laser irradiation (2 W/cm^2) for 5 min. Group 3: Intratumoral injection 100 μL of Bi$_2$S$_3$-AuNCs (C$_{Bi}$ = 4.0 μg/mL). Group 4: Intratumoral injection 100 μL of Bi$_2$S$_3$-AuNCs (C$_{Bi}$ = 4.0 μg/mL) under 808 nm laser irradiation (2 W/cm^2) for 5 min. Group 5: Intratumoral injection 100 μl of Bi$_2$S$_3$ (C$_{Bi}$ = 4.0 μg/mL) +100 μl AuNCs (C$_{Au}$ = 47 μg/mL). Group 6: Intratumoral injection 100 μl of Bi$_2$S$_3$ (C$_{Bi}$ = 4.0 μg/mL) +100 μL AuNCs (C$_{Au}$ = 47 μg/mL) under 808 nm laser irradiation (2 W/cm^2) for 5 min.

Photothermal efficiency was tested by recording the surface tem-perature of the tumor at 0 min, 1 min, 2 min, 3 min, 4 min and 5 min under 808 nm laser irradiation after intratumoral injection of Bi$_2$S$_3$-

AuNCs in tumor-bearing mice.

2.3.7. Fluorescence imaging

Tumor-bearing mice were injected with 100 μL of Bi$_2$S$_3$-AuNCs (C$_{Bi}$ = 4.0 μg/mL), Fluorescence imaging were tested at 0 h, 1 h, 4 h and 8 h. Fluorescence intensity is quantified by using the Living image software (PerkinElmer) to measure the region of interest (ROI).

2.3.8. Histological analysis

At the end of treatment, heart, liver, spleen, lung and kidney were taken, fixed with 4 % formalin for more than 24 h, and treated with conventional paraffin. H&E staining was performed to evaluate the histopathological toxicity.

3. Results and discussion

Fluorescent Bi$_2$S$_3$-AuNCs with PTT were prepared by using BSA as reducer and stabilizer. In this process, Bi^{3+} and Au^{3+} underwent in situ reduction and growth, and then formed fluorescent Bi$_2$S$_3$-AuNCs by optimizing the amount of Bi^{3+} and Au^{3+}. It was noted that BSA with high concentration in alkali solution (pH = 12) was critical to get the
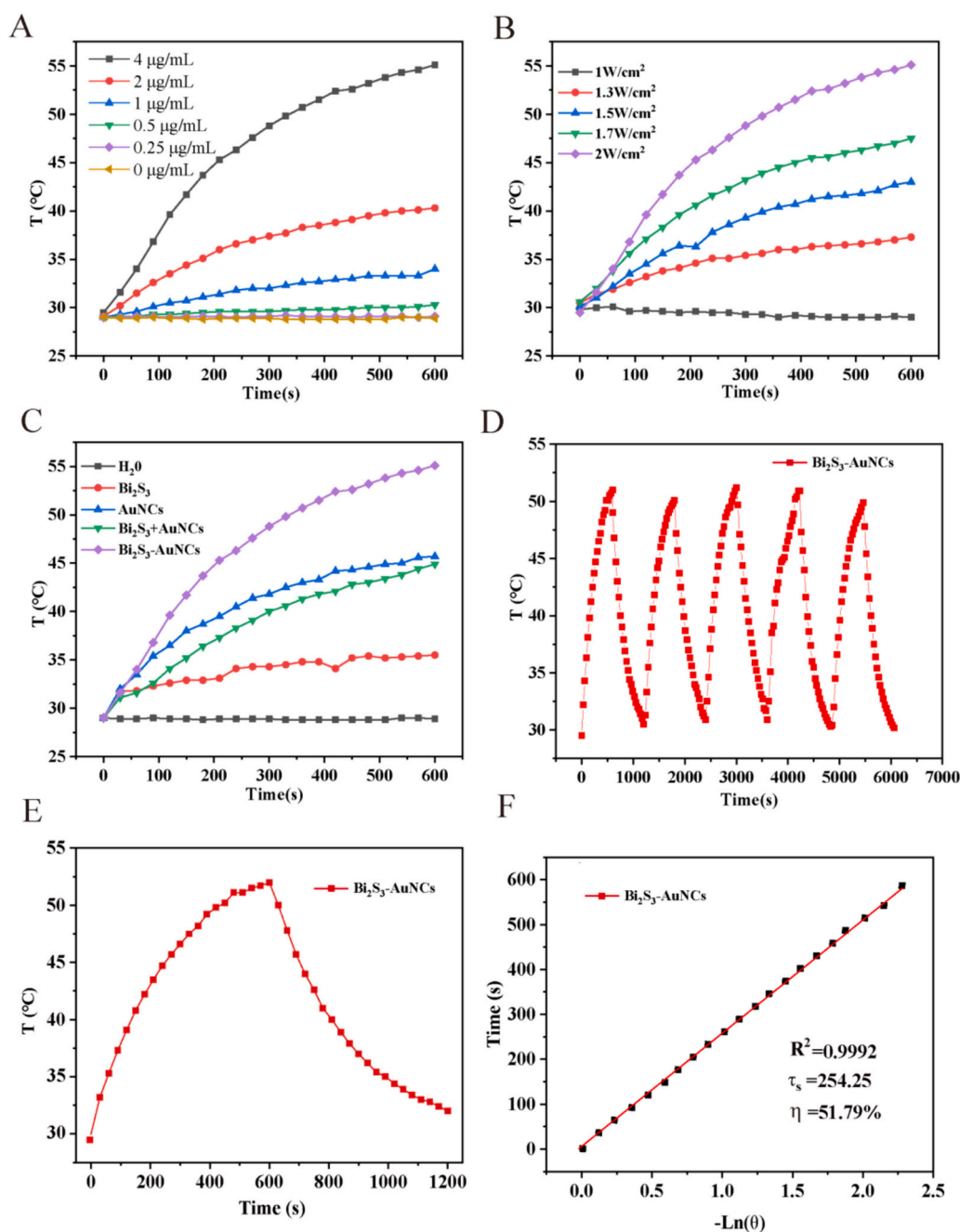
**Fig. 3.** Temperature elevation curves of Bi$_2$S$_3$-AuNCs (A) at various concentrations (C$_{Bi}$ = 0, 0.25, 0.50, 1.00, 2.00 and 4.0 µg/mL) under 808 nm (2 W/cm^2) irradition, (B) under different power densities of 808 nm laser irradiation (C$_{Bi}$ = 4.00 µg/mL). (C) Temperature elevation curves of different nanoparticles under 808 nm (2 W/cm^2) irradition (4.0 µg/mL for Bi, 47 µg/mL for Au, consistent with their rations in Bi$_2$S$_3$-AuNCs); (D) the photothermal profiles of Bi$_2$S$_3$-AuNCs solution (C$_{Bi}$ = 4.00 µg/mL) over five successive cycles under 808 nm (2 W/cm^2) irradition. (E) Heating up and cooling curve of Bi$_2$S$_3$-AuNCs (C$_{Bi}$ = 4.00 µg/mL). (F) Linear cooling time of Bi$_2$S$_3$-AuNCs and -Ln (θ).

fluorescent Bi$_2$S$_3$-AuNCs with PTT. That was because the conformation of BSA was changed with pH. BSA was negatively charged in alkaline, binding Au^{3+} ions by electrostatic interaction. After nucleation, Au^{3+} was reduced to Au^0 by BSA in situ. At pH = 12, the sulphur groups of the cysteine in BSA were exposed in the secondary structur due to BSA unfolding with a decrease in the α-helix and β-sheet contents as well as an increase in random coil conformations. Then Au—S and Bi—S bonds were generated from the strong interaction between Au or Bi and BSA to form Bi$_2$S$_3$-AuNCs (Ma et al., 2014). Transmission Electron Microscope (TEM) showed the uniform morphology with the overall size was about 70 nm **(Fig. S1)**. To reveal the composition, corresponding elemental distribution mapping of Bi$_2$S$_3$-AuNCs was analyzed by Scanning

Transmission Electron Microscopy (STEM). Specifically, the clear morphology images were obtained from the Bright Field (Fig. 1A) and High Angle Annular Dark Field (Fig. 1B). The element mapping showed Bi$_2$S$_3$-AuNCs consist of both Bi and Au element. Au was mainly distributed in the 'head' part of the nanoparticles **(red color, Fig. 1C)** while Bi uniformly distributed in the whole parts of the nanomaterials **(green color, Fig. 1D)**. In FTIR spectrum, the peak at 1652 cm^{-1} represents α helix in the BSA. The peaks at 3435 cm^{-1}, 2958 cm^{-1}, 1530 cm^{-1} and 1400 cm^{-1} corresponded to the characteristic peak of the primary amine, the stretching vibrations of the carbonhydrogen bonds, amide II and COO$^-$, respectively **(Fig. S2 A)**. XRD result also confirmed the successful synthesis of Bi$_2$S$_3$-AuNCs (Fig. 1E). In addition, Au and Bi
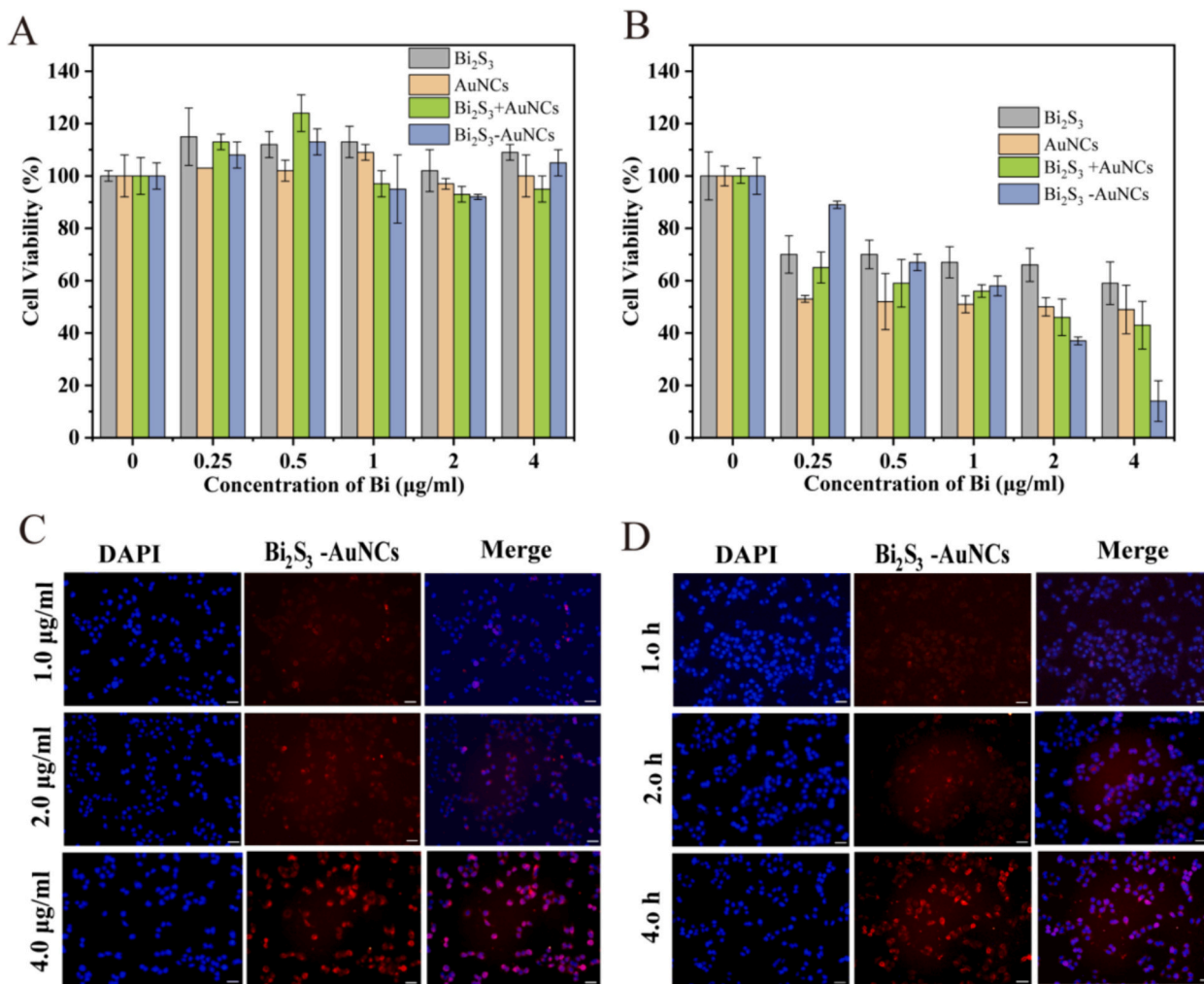
Fig. 4. (A) Biocompatibility of Bi_2S_3, AuNCs, Bi_2S_3 + AuNCs and Bi_2S_3-AuNCs with different concentrations. (B) Biocompatibility of Bi_2S_3, AuNCs, Bi_2S_3 + AuNCs and Bi_2S_3-AuNCs with different concentrations under NIR (at 808 nm, 2 W/cm² of NIR). Cellular endocytosis of Bi_2S_3-AuNCs by B16F10 cells at varied (C) concentration (C_{Bi} = 1.0, 2.0 and 4.0 μg/mL, incubation for 8 h) and (D) time (1, 2 and 4 h, C_{Bi} = 4.0 μg/mL).

element oxidation states were characterized by X-ray photo-electronspectroscopy (Fig. 1F, S2B, S2C, S2D). Au XPS spectrum exhibited two contributions, Au4f7/2 and Au4f5/2, located at 84.0 and 87.8 eV respectively, which can be assigned to Au (0) (Fig. S2B). Similarly, the signal at around 163.4 eV which could be attributed to S2p in both Bi_2S_3 and BSA, and the binding energy at 158.5 eV was assigned to Bi_2S_3 (Fig. S2c). Moreover, Fig. 1F and S2D suggested the presence of N, Bi, and Au elements. Thermal gravimetric (TGA, Fig. S3) analysis showed the weight loss of the as-prepared Bi_2S_3-AuNCs which attributed to the loss of H_2O, and BSA surfactant respectively. Moreover, Inductively Coupled Plasma Optical Emission Spectrometer (ICP-OES) analysis showed that the ratio of Bi: Au was 1: 47.

UV–vis spectra of different concentrations of Bi_2S_3-AuNCs were examined (Fig. 2A), which demonstrated that the absorption value increases with the concentration goes up, and a good linear relationship between concentrations and absorption was also observed (insert in Fig. 2A). Furthermore, Fig. S4A showed the hydrodynamic size of Bi_2S_3-AuNCs (110.4 d.nm), which was accordance with TEM results. The zeta potential was tested to be about −30.4 eV, demonstrating the good stability of the as-prepared Bi_2S_3-AuNCs. To further assess the stability of Bi_2S_3-AuNCs, freeze-dried powder was dissolved in the pure water, PBS solution and DMEM respectively (Fig. 2B). The UV–vis spectra of Bi_2S_3-AuNCs with no significant changes in different solvents indicated that the nanomaterial had good stability. As shown in Fig. 2C and D,

Bi_2S_3-AuNCs emitted an intense red florescence under 365 nm UV light. The fluorescence of the as-prepared materials was attributed to the formation of AuNCs. According to previous report, Au25NCs (composed of 25 Au atoms) was formed under the structural regulation of BSA at pH = 12. The spatial confinement of free electrons in subnanometer dimensions of AuNCs resulted in discrete and size-tunable electronic transitions, leading to molecular-like red fluorescence property (Chen et al., 2023a). It should be noted that the fluorescence brightness of Bi_2S_3-AuNCs was effected by the amount of $Bi(NO_3)_3 \cdot 5H_2O$ while keep other conditions unchanged. It showed that the fluorescence of Bi_2S_3-AuNCs was dramatically decreased when prepared with 1.25 mg of $Bi(NO_3)_3 \cdot 5H_2O$. It may be attributed to the increase of semiconductors Bi_2S_3 which could quench the florescence of AuNCs. Then the fluorescence intensity was evaluated by fluorescence spectrophotometer. As revealed in Fig. S5 and 2E, the Bi_2S_3-AuNCs showed excitation and emission peaks at 505 nm and 670 nm, respectively. Compared with AuNCs prepared by BSA (λex = 480 nm, λem = 640 nm), the red shift can be found in the excitation/emission wavelength of Bi_2S_3-AuNCs. This may be due to the introduction of the semiconductor nanomaterials Bi_2S_3 which infect the the electronic energy of gold nanoclusters. It was accordance with the previous reports (Zhao et al., 2020). Moreover, a significant increase in the fluorescence intensity can be seen as the concentration increases, indicating that Bi_2S_3-AuNCs nanomaterial has the highest fluorescence intensity. Importantly, there is a good linear
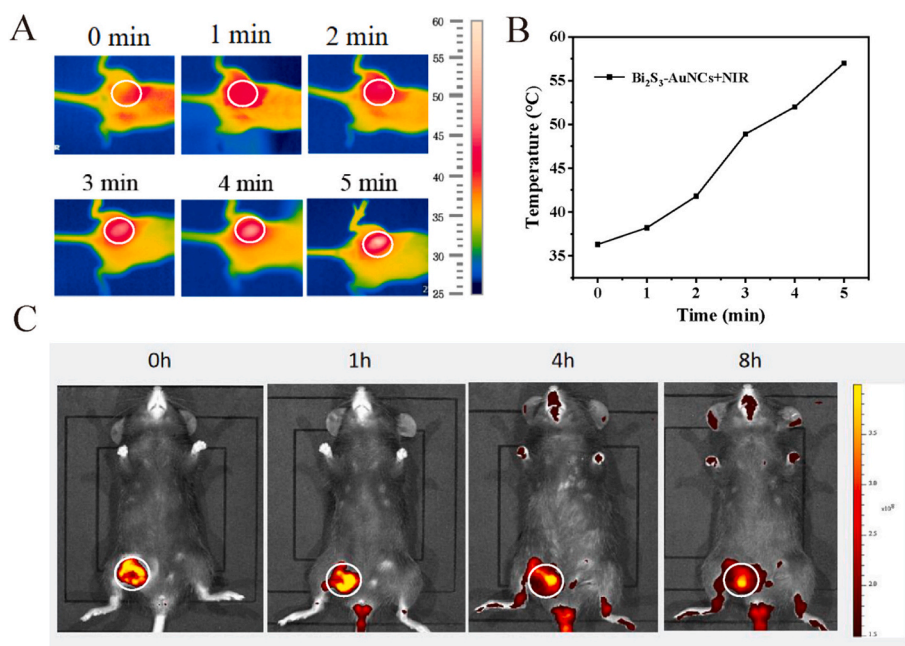
Fig. 5. (A) Infrared thermal imaging maps at different time points of tumor-bearing mice with laser irradiation (at 808 nm, 2 W/cm^2 of NIR) after injection of Bi$_2$S$_3$-AuNCs (Circles represent the tumor sites). (B) Temperature elevation profiles in tumor area. (C) In vivo fluorescence imaging of tumor-bearing mice at 0 h, 1 h, 4 h and 8 h after injection of Bi$_2$S$_3$-AuNCs (λ_{ex} = 500 nm, λ_{em} = 670 nm, circles represent the tumor sites).

relationship between the fluorescence intensity and concentration (Fig. 2F), suggesting that Bi$_2$S$_3$-AuNCs have the potential to act as an ideal fluorescence imaging agent for imaging-guided cancer treatment.

To investigate the photothermal performance of the as-prepared Bi$_2$S$_3$-AuNCs, temperature elevation curves were examined first. It showed that temperature rose as the concentrations increased, and the temperature could reached to 55.1 °Cat the concentration of 4.00 μg/mL (Fig. 3A). Similarly, the temperature increase had the same trend under different power densities (Fig. 3B). Apart from this, the temperature of AuNCs and Bi$_2$S$_3$ + AuNCs (C$_{Bi}$ = 4.0 μg/mL, C$_{Au}$ = 47 μg/mL) were increased to 45.7 °C and 44.9 °C, respectively. Bi$_2$S$_3$ NPs and AuNCs could not lead to effective temperature rise. Interestingly, Bi$_2$S$_3$-AuNCs with the same concentration of Au and Bi have the highest temperature rise compared with the other groups (Fig. 3C), suggesting the unique photothermal performance of Bi$_2$S$_3$-AuNCs. It may be due to the coordination of Au and Bi$_2$S$_3$ in Bi$_2$S$_3$-AuNCs which was formed by the structural regulation of BSA. It was accordance with our previous report (Zhao et al., 2020). Importantly, after five photothermal cycles of NIR irradiation, no temperature rise changed significantly in the Bi$_2$S$_3$-AuNCs, AuNCs, and Bi$_2$S$_3$ + AuNCs groups, showing good photostability of the these materials. But the temperature decreased in the Bi$_2$S$_3$ group from the third cycle. (Fig. 3D and S6). The photothermal conversion efficiencies of Bi$_2$S$_3$-AuNCs, Bi$_2$S$_3$, AuNCs and Bi$_2$S$_3$ + AuNCs were calculated as 51.79 %, 16.83 %, 39.01 %, and 38.87 %, respectively. The photothermal conversion efficiency of Bi$_2$S$_3$-AuNCs was the highest, indicating that Bi$_2$S$_3$-AuNCs had effective photothermal activity (Fig. 3E, F and S7). The above results revealed that Bi$_2$S$_3$-AuNCs has potential to act as effective photothermal agent in the treatment of cancers.

MTT experiment was employed to evaluate the biocompatibility of Bi$_2$S$_3$-AuNCs. As shown in Fig. 4A, cell death of each experimental group was all lower than 10 %, suggesting that the as-prepared nanomaterial had a good biocompatibility. Inspired by the result, photothermal property was also checked in vitro (Fig. 4B). The value of cell viability of each group decreased with the concentration increased. Specifically, the cell viability of Bi$_2$S$_3$-AuNCs under 808 nm irradiation was lowest than that of other groups, which was consisted with the result of the above photothermal assessment. The result also confirmed that Bi$_2$S$_3$-AuNCs

had excellent photothermal performance.

Therefore, intracellular uptake efficacy was conducted to examine the fluorescent performance of Bi$_2$S$_3$-AuNCs after incubating with B16F10 cell. Fig. 4C showed that the intensity of red florescence from the as-prepared Bi$_2$S$_3$-AuNCs became much higher with the concentration increased (C$_{Bi}$ = 1.0, 2.0 and 4.0 μg/mL) after 8 h of incubation. Bi$_2$S$_3$-AuNCs entered cells after incubation for 1 h, and the internalized amount of Bi$_2$S$_3$-AuNCs increased commensurately with the extended incubation duration (Fig. 4D, Fig. S8). About 31.7 % of Bi$_2$S$_3$-AuNCs could enter into B16F10 cells when the uptake time was 8 h at the concentration of C$_{Bi}$ = 4.0 μg/mL, indicating that the as-prepared Bi$_2$S$_3$-AuNCs had the potential for the fluorescence imaging. The mechanism for Bi$_2$S$_3$-AuNCs entering the cells may be attributed to an energy-dependent process named endocytosis. That is the uptake of substances from the extracellular environment by vesicles generated from the cell plasma membrane (Manzanares and Ceña, 2020).

To demonstrate the photothermal effect of Bi$_2$S$_3$-AuNCs in vivo, tumor-bearing mice were irradiated with 808 nm laser after intratumoral injection of PBS, Bi$_2$S$_3$, AuNCs, Bi$_2$S$_3$ + AuNCs and Bi$_2$S$_3$-AuNCs. As shown in Fig. 5A, B and Fig. S10, the surface temperature of the tumor site in group Bi$_2$S$_3$-AuNCs gradually increased with time, and the temperature could increased from 35.9 to 56.4 °C after 5 min of laser irradiation. For other groups, the temperature in PBS and Bi$_2$S$_3$ groups increased slightly while that in AuNCs and Bi$_2$S$_3$ + AuNCs groups increased no more than 46 °C, which was accordance with the results in Fig. 3C. It indicated that Bi$_2$S$_3$-AuNCs could act as photothermal agents to heat tumor areas under 808 nm laser irradiation (2 W/cm^2 of NIR). After PBS, Bi$_2$S$_3$, AuNCs, Bi$_2$S$_3$ + AuNCs and Bi$_2$S$_3$-AuNCs were injected into tumor-bearing mice, fluorescence images at different time intervals were collected (Fig. 5C and Fig. S11). It showed that the fluorescence for Bi$_2$S$_3$ + AuNCs and Bi$_2$S$_3$-AuNCs groups was a little weaker than that of AuNCs group, probably as the florescence of AuNCs was quenched by Bi$_2$S$_3$ nanoparticles due to the electron transition from AuNCs to Bi$_2$S$_3$ nanoparticles. However, strong intratumoral fluorescence was still observed in Bi$_2$S$_3$-AuNCs group even after 8 h injection, confirming that the as-prepared material could be used for fluorescence imaging to guide cancer therapy.

The set-up of the treatment was illustrated in Fig. 6A. The trends of
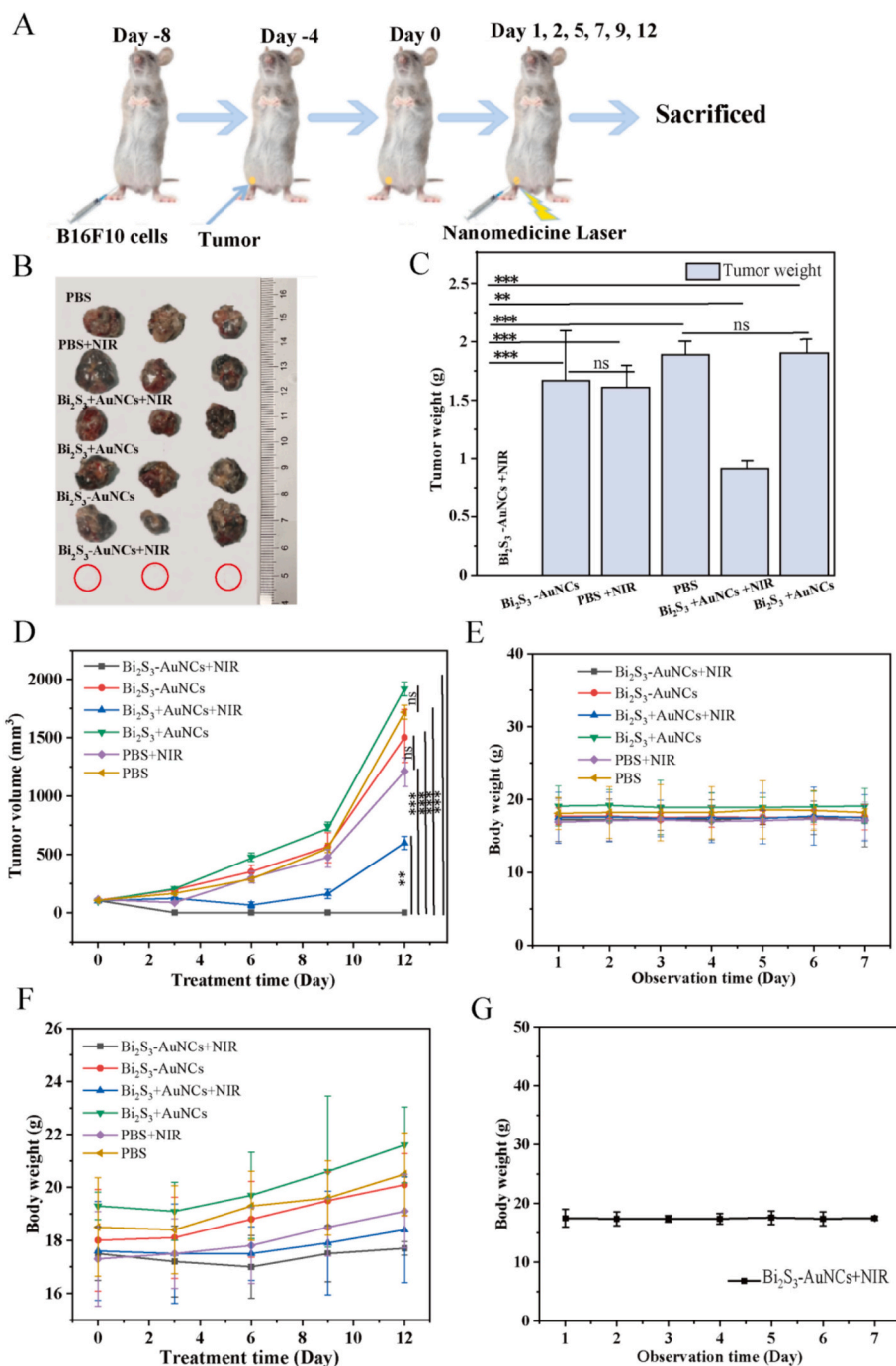
Fig. 6. (A) Schematic illustration of the in vivo therapeutic process. (B) Photographs of tumors, (C) Tumor weights and (D) tumor relative volume after different treatments. Body weight of mice in each group (E) one week before treatment and (F) during the 12-day treatment period. (G) The body weight of mice treatment with Bi_2S_3-AuNCs+NIR group after cure. **$P < 0.01$, and ***$P < 0.001$, ns, not statistically significant.

tumor growth apparently changed during different treatment groups (Fig. 6B-D). The tumor treated with PBS and other groups without NIR grew rapidly. The tumor growth of the mixture of Bi_2S_3 and AuNCs under NIR irradiation was inhibited at the beginning, but the tumor recurrence was observed after 5 days of treatment. It is worth noting that Bi_2S_3-AuNCs+NIR group significantly suppressed tumor growth by achieving a synergistic effect. Importantly, the skin in Bi_2S_3-AuNCs + NIR group gradually grew hair after 9 days, and no tumor recurrence was observed after 12 days treatment, indicating that the excellent treatment of cancer. As can be seen from Fig. 6E, the body weight of mice in each group was basically unchanged one week before the experiment. However, the body weight of mice in all groups except Bi_2S_3-AuNCs+NIR group was increased probably due to the growth of tumor (Fig. 6F). According to Fig. 6G, the body weight of mice in Bi_2S_3-AuNCs+NIR group remained stable after one week of treatment, which further indicated that high performance of the Bi_2S_3-AuNCs+NIR group. Vital organs were harvested 12 days after treatment and stained with hematoxylin and eosin (H&E). The H&E staining analysis of the main organs of Bi_2S_3-AuNCs+NIR group showed that there was no obvious acute pathological toxicity and tissue damage or inflammatory damage during the treatment, confirming that the potential application of the as-prepared Bi_2S_3-AuNCs for photothermal therapy of cancer (Fig. 7).
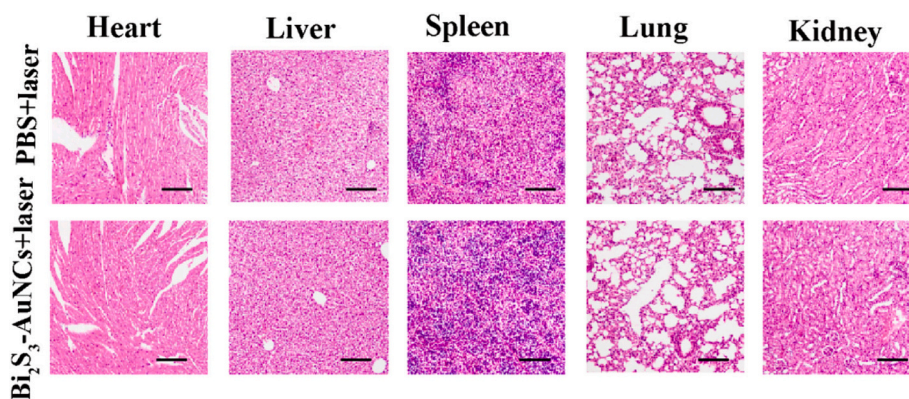
Fig. 7. H&E staining of heart, liver, spleen, lung, and kidney tissue slices from tumor-bearing mice that received different treatments under laser (808 nm, 2 W/cm^2) for 12 days (scale bar = 100 μm).

4. Conclusion

In conclusion, Bi$_2$S$_3$-AuNCs was developed for fluorescence/infrared thermal imaging guided photothermal therapy as the first example. The Bi$_2$S$_3$-AuNCs with good cytocompatibility could accumulate at the tumor site and exhibited considerable visual fluorescence imaging and infrared thermal imaging, which provided an extended therapeutic window for photothermal therapy. The inhibition of tumor in vivo confirmed the excellent photothermal therapeutic ability of Bi$_2$S$_3$-AuNCs under NIR irradiation and thus is expected to play a role as a precision nanodiagnostic agent in future.

CRediT authorship contribution statement

Hongmei Sun: Writing – review & editing, Supervision, Methodology, Funding acquisition, Conceptualization. **Yuyu Cao:** Writing – original draft, Visualization, Methodology, Investigation, Formal analysis, Data curation. **Beibei Zhai:** Methodology, Investigation, Formal analysis, Data curation. **Xiaoshuang Zhao:** Software, Methodology, Investigation. **Xuejun Zhang:** Software, Investigation. **Jiangtao Su:** Writing – review & editing, Supervision, Project administration.

Declaration of competing interest

The authors declare that they have no known competing financial interests or personal relationships that could have appeared to influence the work reported in this paper.

Data availability

Data will be made available on request.

Acknowledgement

Appendix A. Supplementary data

Supplementary data to this article can be found online at https://doi.org/10.1016/j.ijpx.2024.100286.

References

Ai, K., Liu, Y., Liu, J., Yuan, Q., He, Y., Lu, L., 2011. Large-scale synthesis of Bi(2)S(3) nanodots as a contrast agent for in vivo X-ray computed tomography imaging. Adv. Mater. 23 (42), 4886–4891. https://doi.org/10.1002/adma.201103289.

Alibakhshi, A., Abarghooi Kahaki, F., Ahangarzadeh, S., Yaghoobi, H., Yarian, F., Arezumand, R., Ranjbari, J., Mokhtarzadeh, A., de la Guardia, M., 2017. Targeted cancer therapy through antibody fragments-decorated nanomedicines. J. Control. Release 268, 323–334. https://doi.org/10.1016/j.jconrel.2017.10.036.

Baranwal, J., Barse, B., Di Petrillo, A., Gatto, G., Pilia, L., Kumar, A., 2023. Nanoparticles in Cancer Diagnosis and Treatment. Materials 16 (15). https://doi.org/10.3390/ma16155354.

Bobo, D., Robinson, K.J., Islam, J., Thurecht, K.J., Corrie, S.R., 2016. Nanoparticle-based Medicines: a Review of FDA-Approved Materials and Clinical Trials to date. Pharm. Res. 33 (10), 2373–2387. https://doi.org/10.1007/s11095-016-1958-5.

Chai, J., Zhu, J., Tian, Y., Yang, K., Luan, J., Wang, Y., 2023. Carbon monoxide therapy: a promising strategy for cancer. J. Mater. Chem. B 11 (9), 1849–1865. https://doi.org/10.1039/d2tb02599j.

Chansaenpak, K., Yong, G.Y., Prajit, A., Hiranmartsuwan, P., Selvapaandian, S., Ouengwanarat, B., Khrootkaew, T., Pinyou, P., Kue, C.S., Kamkaew, A., 2023. Aza-BODIPY-based polymeric nanoparticles for photothermal cancer therapy in a chicken egg tumor model. Nanoscale Adv. https://doi.org/10.1039/d3na00718a.

Chen, Q., Wen, J., Li, H., Xu, Y., Liu, F., Sun, S., 2016. Recent advances in different modal imaging-guided photothermal therapy. Biomaterials 106, 144–166. https://doi.org/10.1016/j.biomaterials.2016.08.022.

Chen, L., Gharib, M., Zeng, Y., Roy, S., Nandi, C.K., Chakraborty, I., 2023a. Advances in bovine serum albumin-protected gold nanoclusters: from understanding the formation mechanisms to biological applications. Mater. Today Chem. 29 https://doi.org/10.1016/j.mtchem.2023.101460.

Chen, Y., Zhou, F., Wang, C., Hu, L., Guo, P., 2023b. Nanostructures as Photothermal Agents in Tumor Treatment. Molecules 28 (1). https://doi.org/10.3390/molecules28010271.

Christie, L.B., Zheng, W., Johnson, W., Marecki, E.K., Heidrich, J., Xia, J., Oh, K.W., 2023. Review of imaging test phantoms. J. Biomed. Opt. 28 (8) https://doi.org/10.1117/1.Jbo.28.8.080903.

de la Fleche, A.N., Atteia, J.-L., Boy, J., Klotz, A., Langlois, A., Larrieu, M., Mathon, R., Valentin, H., Ambert, P., Clemens, J.-C., Dornic, D., Kajfasz, E., Le Graet, J., Llido, O., Secroun, A., Boulade, O., Bounab, A., Badano, G., Gravrand, O., Aufranc, S., Lamoure, A., Martineau, L., Rubaldo, L., Geoffray, H., Gonzalez, F., Basa, S., Dolon, F., Floriot, J., Lombardo, S., Cuevas, S., Farah, A., Fuentes, J., Langarica, R., Watson, A.M., Butler, N., 2023. CAGIRE: a wide-field NIR imager for the COLIBRI 1.3 meter robotic telescope. Exp. Astron. https://doi.org/10.1007/s10686-023-09903-x.

Deng, G., Yao, L., Chen, M., Yang, Y., Lu, S., Wu, G., 2023. The Photothermal Conversion and UV Resistance of Silk Fabrics Being Achieved through Surface Modification with C@SiO$_2$ Nanoparticles. Molecules 28 (24). https://doi.org/10.3390/molecules28247970.

Djajakusumah, T.M., Candrawinata, V.S., Ho, J.P., Herman, H., Lukman, K., Lesmana, R., 2023. The predictive value of infrared thermal imaging (IRT) for peripheral artery disease: a systematic review. Medicine 102 (43). https://doi.org/10.1097/md.0000000000035639.

Dong, J., Li, X., Zhou, S., Liu, Y., Deng, L., Chen, J., Hou, J., Hou, C., Huo, D., 2023. CRISPR/Cas12a-Powered EC/FL Dual-Mode Controlled-Release Homogeneous Biosensor for Ultrasensitive and Cross-Validated Detection of Messenger Ribonucleic Acid. Anal. Chem. 95 (32), 12122–12130. https://doi.org/10.1021/acs.analchem.3c02335.

Du, R., Zhao, Z., Cui, J., Li, Y., 2023. Manganese-based Nanotheranostics for magnetic Resonance Imaging-Mediated Precise Cancer Management. Int. J. Nanomedicine 18, 6077–6099. https://doi.org/10.2147/ijn.S426311.

Freitas, S.C.C., Sanderson, D., Caspani, S., Magalhaes, R., Cortes-Llanos, B., Granja, A., Reis, S., Belo, J.H., Azevedo, J., Gomez-Gaviro, M.V., de Sousa, C.T., 2023. New Frontiers in Colorectal Cancer Treatment Combining Nanotechnology with Photo- and Radiotherapy. Cancers 15 (2). https://doi.org/10.3390/cancers15020383.

Guhaniyogi, L., 2023. The Impact of the Emergency Presentation of patients Diagnosed with Lung Cancer on Treatment Outcomes in Wales. J. Thorac. Oncol. 18 (11), S739.

Hu, S., Huang, L., Zhou, L., Wu, T., Zhao, S., Zhang, L., 2023. Single-Excitation Triple-Emission Down-/Up-Conversion Nanoassemblies for Tumor Microenvironment-

Enhanced Ratiometric NIR-II Fluorescence Imaging and Chemo-/Photodynamic Combination Therapy. Anal. Chem. 95 (7), 3830–3839. https://doi.org/10.1021/acs.analchem.2c05333.

Jiang. Y., Cao Y., Wu. J., Bai. R.,Wan. S., Dai.L., Su. J., Sun. H., 2024. Au nanozyme-based multifunctional hydrogel for inflammation visible monitoring and treatment. Materials Taoday Bio.doi:https://doi.org/10.1039/j.mtbio.2024.100960.

Katifelis, H., Gazouli, M., 2021. Cancer-Targeted Nanotheranostics: recent advances and Future Perspectives. Cancer Nanotheranostics 97–115.

Liu, Y., Bhattarai, P., Dai, Z., Chen, X., 2019. Photothermal therapy and photoacoustic imaging via nanotheranostics in fighting cancer. Chem. Soc. Rev. 48 (7), 2053–2108. https://doi.org/10.1039/c8cs00618k.

Ma, X., Wen, X., Huang, K., Tang, J., Yu, P., 2014. Dynamic study on the transformation process of gold nanoclusters Nanotechnology. Nanotechnology. https://doi.org/10.1088/0957-448/25/44/44/445705.

Manzanares, D., Ceña, V., 2020. Endocytosis: the Nanoparticle and Submicron Nanocompounds Gateway into the Cell. Pharmaceutics. https://doi.org/10.3390/pharmaceutics12040371.

Nguyen, N.P., Ali, A., Vinh-Hung, V., Gorobets, O., Chi, A., Mazibuko, T., Migliore, N., Vasileiou, M., Lehrman, D., Mohammadianpanah, M., Javadinia, S.A., Loganadane, G., Basu, T., Bose, S., Karlsson, U., Giap, H., 2023. Stereotactic Body Radiotherapy and Immunotherapy for older patients with Oligometastases: a Proposed Paradigm by the International Geriatric Radiotherapy Group. Cancers 15 (1). https://doi.org/10.3390/cancers15010244.

Nosrati, H., Attari, E., Abhari, F., Barsbay, M., Ghaffarlou, M., Mousazadeh, N., Vaezi, R., Kavetskyy, T., Rezaeejam, H., Webster, T.J., Johari, B., Danafar, H., 2022. Complete ablation of tumors using synchronous chemoradiation with bimetallic theranostic nanoparticles. Bioact. Mater. 7, 74–84. https://doi.org/10.1016/j.bioactmat.2021.05.015.

Roncevic, A., Koruga, N., Koruga, A.S., Roncevic, R., Rotim, T., Simundic, T., Kretic, D., Peric, M., Turk, T., Stimac, D., 2023. Personalized Treatment of Glioblastoma: Current State and Future Perspective. Biomedicines 11 (6). https://doi.org/10.3390/biomedicines11061579.

Sheng, P., Bu, C., Hui, T., Zhou, L., Chen, H., Zhou, G., 2023. Polydopamine-activated celastrol carbon dots for synergistic chemotherapy-photothermal therapy of tumors. International Journal of Pharmaceutics-X 6. https://doi.org/10.1016/j.ijpx.2023.100218.

Siegel, R.L., Miller, K.D., Fuchs, H.E., Jemal, A., 2022. Cancer statistics, 2022. CA Cancer J. Clin. 72 (1), 7–33. https://doi.org/10.3322/caac.21708.

Thapa, P., Singh, V., Gupta, K., Shrivastava, A., Kumar, V., Kataria, K., Mishra, P.R., Mehta, D.S., 2023. Point-of-care devices based on fluorescence imaging and spectroscopy for tumor margin detection during breast cancer surgery: Towards breast conservation treatment. Lasers Surg. Med. 55 (4), 423–436. https://doi.org/10.1002/lsm.23651.

Todd, B., 2023. New Study: poverty is a leading Cause of death in the United States. Am. J. Nurs. 123 (8), 15. https://doi.org/10.1097/01.Naj.0000947420.26517.98.

Wang, J., Wu, X., Shen, P., Wang, J., Shen, Y., Shen, Y., Webster, T.J., Deng, J., 2020. Applications of Inorganic Nanomaterials in Photothermal Therapy based on Combinational Cancer Treatment. Int. J. Nanomedicine 15, 1903–1914. https://doi.org/10.2147/IJN.S239751.

Wang, Y., Liu, X.-l., Zhang, Q.-z., Wang, C., Huang, S.-y., Liu, Y.-n., Yu, T., Yang, R.-q., Chen, G.-z., Chaker, Mohamed, Ma, D.-L., 2023. Stable, Cost-Effective TiN-Based Plasmonic Nanocomposites with over 99% Solar Steam Generation Efficiency. Adv. Mater. 33 https://doi.org/10.1002/adfm.202212301.

Wen, S., Ovais, M., Li, X., Ren, J., Liu, T., Wang, Z., Cai, R., Chen, C., 2022. Tailoring bismuth-based nanoparticles for enhanced radiosensitity in cancer therapy. Nanoscale 14 (23), 8245–8254. https://doi.org/10.1039/d2nr01500e.

Wu, G.-L., Liu, F., Li, N., Fu, Q., Wang, C.-K., Yang, S., Xiao, H., Tang, L., Wang, F., Zhou, W., Wang, W., Kang, Q., Li, Z., Lin, N., Wu, Y., Chen, G., Tan, X., Yang, Q., 2023. Trisulfide Bond-Mediated Molecular Phototheranostic Platform for "Activatable" NIR-II Imaging-Guided Enhanced Gas/Chemo-Hypothermal Photothermal Therapy. Adv. Sci. https://doi.org/10.1002/advs.202304104.

Yang, Z., Wang, L., Zhang, J., Liu, J., Yu, X., 2023. Application of bismuth sulfide based nanomaterials in cancer diagnosis and treatment. Nano Today 49. https://doi.org/10.1016/j.nantod.2023.101799.

Zhang, R., Xu, Y., Zhang, Y., Kim, H.S., Sharma, A., Gao, J., Yang, G., Kim, J.S., Sun, Y., 2019. Rational design of a multifunctional molecular dye for dual-modal NIR-II/photoacoustic imaging and photothermal therapy. Chem. Sci. 10 (36), 8348–8353. https://doi.org/10.1039/c9sc03504d.

Zhao, X., Li, S., Huang, T., Sun, H., Zhu, H., Guo, H., Liu, M., 2020. Synthesis of au/Bi$_2$S$_3$ nanoflowers for efficient photothermal therapy. New J. Chem. 44 (43), 18724–18731. https://doi.org/10.1039/d0nj04313c.

Zheng, X., Shi, J., Bu, Y., Tian, G., Zhang, X., Yin, W., Gao, B., Yang, Z., Hu, Z., Liu, X., Yan, L., Gu, Z., Zhao, Y., 2015. Silica-coated bismuth sulfide nanorods as multimodal contrast agents for a non-invasive visualization of the gastrointestinal tract. Nanoscale 7 (29), 12581–12591. https://doi.org/10.1039/c5nr03068d.